

SMA and *Spitzer* Observations of Bok Globule CB 17: A Candidate First Hydrostatic Core?

Xuepeng Chen¹, Héctor G. Arce¹, Michael M. Dunham¹, Qizhou Zhang², Tyler L. Bourke²,
Ralf Launhardt³, Markus Schmalzl³, and Thomas Henning³

¹*Department of Astronomy, Yale University, Box 208101, New Haven, CT 06520-8101, USA; xuepeng.chen@yale.edu*

²*Harvard-Smithsonian Center for Astrophysics, 60 Garden Street, Cambridge, MA 02138, USA*

³*Max Planck Institute for Astronomy, Königstuhl 17, D-69117 Heidelberg, Germany*

ABSTRACT

We present high angular resolution SMA and *Spitzer* observations toward the Bok globule CB 17. SMA 1.3 mm dust continuum images reveal within CB 17 two sources with an angular separation of $\sim 21''$ (~ 5250 AU at a distance of ~ 250 pc). The northwestern continuum source, referred to as CB 17 IRS, dominates the infrared emission in the *Spitzer* images, drives a bipolar outflow extending in the northwest-southeast direction, and is classified as a low luminosity Class 0/I transition object ($L_{\text{bol}} \sim 0.5 L_{\odot}$). The southeastern continuum source, referred to as CB 17 MMS, has faint dust continuum emission in the SMA 1.3 mm observations ($\sim 6\sigma$ detection; ~ 3.8 mJy), but is not detected in the deep *Spitzer* infrared images at wavelengths from 3.6 to $70 \mu\text{m}$. Its bolometric luminosity and temperature, estimated from its spectral energy distribution, are $\leq 0.04 L_{\odot}$ and ≤ 16 K, respectively. The SMA CO (2–1) observations suggest that CB 17 MMS may drive a low-velocity molecular outflow ($\sim 2.5 \text{ km s}^{-1}$), extending in the east-west direction. Comparisons with prestellar cores and Class 0 protostars suggest that CB 17 MMS is more evolved than prestellar cores but less evolved than Class 0 protostars. The observed characteristics of CB 17 MMS are consistent with the theoretical predictions from radiative/magneto hydrodynamical simulations of a first hydrostatic core, but there is also the possibility that CB 17 MMS is an extremely low luminosity protostar deeply embedded in an edge-on circumstellar disk. Further observations are needed to study the properties of CB 17 MMS and to address more precisely its evolutionary stage.

Subject headings: ISM: clouds — ISM: globules — ISM: jets and outflows — ISM: individual (CB 17, L1389) — stars: formation

1. INTRODUCTION

Our knowledge of the formation and evolution of low-mass stars has made significant progress over the past two decades (see, e.g., Reipurth et al. 2007 for several reviews). It is widely accepted that low-mass stars form from the gravitational collapse of dense molecular cores (e.g., Shu et al. 1987). Initially, these cores, generally referred to as prestellar cores, are cold dense condensations with infall motions, where no central stellar object yet exists (André et al. 2009). Resulting from the collapse of prestellar cores, Class 0 objects are the youngest accreting protostars observed right after point mass formation, when most of the mass of the system is still in the surrounding dense core/envelope (André et al. 2000). Representing the earliest phase of low-mass star formation, both prestellar cores and Class 0 protostars have been extensively observed and studied using (sub) millimeter and infrared telescopes (see, e.g., reviews by Di Francesco et al. 2007; Ward-Thompson et al. 2007). However, despite all of the observational advances in the past two decades, we still do not have a good understanding of the evolutionary process that turns a prestellar core into a protostar. This is illustrated by the fact that several “prestellar” cores, like L1014 and L1521F, were found to harbor very low-luminosity protostars in sensitive infrared observations (see Young et al. 2004; Bourke et al. 2006). A better understanding of the star formation process can only be achieved by studying the detailed properties of cores and their surroundings at different evolutionary stages.

In this paper, we present high angular resolution observations of CB 17, using the Submillimeter Array¹ (SMA; Ho et al. 2004) and the *Spitzer Space Telescope* (*Spitzer*). CB 17 (also known as L1389) is a small and slightly cometary-shaped dark cloud, located near Perseus and associated with the Lindblad ring (Lindblad et al. 1973). It was classified as a Bok globule by Clemens & Barvainis (1988). The distance of CB 17 is somewhat uncertain, ranging from ~ 210 pc (van Leeuwen 2007) to ~ 300 pc (Dame et al. 1987). Following Launhardt et al. (2010), we adopt a distance of 250 ± 50 pc in this work.

The roundish core of the CB 17 globule is associated with a faint and cold IRAS point source (IRAS 04005+5647, detected only at $100 \mu\text{m}$ and $60 \mu\text{m}$). CB 17 has been studied by various groups using different molecular line transitions (e.g., Lemme et al. 1996; Kane & Clemens 1997; Launhardt et al. 1998; Benson et al. 1998; Turner et al. 1997, 2000; Caselli et al. 2002a). The core was found to have a mean kinetic gas temperature of $T_{\text{kin}} \approx 10$ K, and the observed non-thermal widths of optically thin lines are in the range $0.25\text{--}0.45 \text{ km s}^{-1}$.

¹The Submillimeter Array is a joint project between the Smithsonian Astrophysical Observatory and the Academia Sinica Institute of Astronomy and Astrophysics and is funded by the Smithsonian Institution and the Academia Sinica.

(e.g., N_2H^+ , Benson et al. 1998; Caselli et al. 2002a). Numerical simulations based on multi-line observations suggest that the kinematical structure of CB 17 can be explained by a prestellar core with combined subsonic infall, small rotational, and low-level internal turbulent motions (Pavlyuchenkov et al. 2006).

Based on the infrared and single-dish (sub-) millimeter continuum observations, Launhardt et al. (2010) found two sources within the CB 17 globule. One source, referred to as CB 17 IRS, dominates the infrared emission in the *Spitzer* images but has faint millimeter continuum emission. The other source, referred to as CB 17 SMM, has no compact infrared emission in the *Spitzer* images but dominates the millimeter continuum emission. The results from fitting the spectral energy distributions (SEDs) suggested that CB 17 IRS may be a Class 0/I transition object while CB 17 SMM may be a prestellar core. In addition, the IRAM-30m 1.3 mm continuum images suggest that there may be two sub-cores (SMM 1 and SMM 2) in CB 17 SMM with a separation of $14''$, although this result was not confirmed by the less sensitive SCUBA $850\ \mu\text{m}$ images (see Launhardt et al. 2010).

2. OBSERVATIONS AND DATA REDUCTION

2.1. SMA Observations

The SMA 230 GHz observations of CB 17 were carried out in the compact configuration on 2008 November 30 (eight antennas, ~ 6.5 hours integration time) and 2009 December 25 (seven antennas, ~ 3.3 hours integration time). Zenith opacities during the observations were typically in the range of 0.10–0.15. In the 2008 observations, the digital correlator was set up to cover the frequency ranges 219.5–221.4 GHz and 229.5–231.4 GHz in the lower and upper sidebands (LSB and USB), respectively. This setup includes the three isotopic CO lines of ^{12}CO (2–1) (230.538 GHz), ^{13}CO (2–1) (220.399 GHz), and C^{18}O (2–1) (219.560 GHz), as well as N_2D^+ (3–2) (231.322 GHz). The channel widths were set up to be 0.406, 0.406, 0.203, and 0.203 MHz for the four lines, corresponding to the velocity resolutions of ~ 0.50 , ~ 0.50 , ~ 0.25 , and $\sim 0.25\ \text{km s}^{-1}$, respectively. The 1.3 mm continuum emission was recorded with a total bandwidth of ~ 3.5 GHz, combining the line-free portions of the two sidebands (~ 1.7 GHz USB and ~ 1.8 GHz LSB). In the 2009 observations, the SMA bandwidth was upgraded to 4 GHz, and the correlator was set up to cover the approximate frequency range of 216.8–220.8 GHz in the LSB and of 228.8–232.8 GHz in the USB. The total continuum bandwidth is ~ 7.5 GHz (~ 3.8 GHz LSB and ~ 3.7 GHz USB). System temperatures ranged from 100 to 200 K (depending on elevation) in the 2008 observations (typical value ~ 140 K) and from 100 to 150 K in the 2009 observations (typical value ~ 120 K). The SMA primary beam is about $55''$ at 230 GHz.

The visibility data were calibrated with the MIR package (Qi 2005). In the 2008 observations, Saturn and quasar 3c454.3 were used for bandpass calibration, and quasars 0359+509 and 3c111 for gain calibration. In the 2009 observations, quasar 3c273 was used for bandpass calibration, and quasars 3c84 and 0359+509 for gain calibration. Uranus and 3c273 were used for absolute flux calibration in the 2008 and 2009 observations, respectively. We estimate a flux accuracy of $\sim 20\%$, by comparing the final quasar fluxes with the SMA calibration database. The calibrated visibility data were further imaged using the Miriad toolbox (Sault et al. 1995). We combined the 2008 and 2009 dust continuum data together to improve the imaging sensitivity. However, the line results shown in this paper were taken only from the 2008 observations; the reason we did not include the 2009 line data is that the velocity resolution in the 2009 observations was set up to be about 1.0 km s^{-1} uniformly, about two times (in ^{12}CO and ^{13}CO) or four times (in C^{18}O and N_2D^+) larger than that of the 2008 line data. It must be noted that the line results taken in the 2008 and 2009 observations are consistent with each other. Table 1 lists the SMA synthesized beam size and theoretical noise levels at 1.3 mm continuum and in the CO (2–1) line, with robust uv weighting 1.0.

2.2. *Spitzer* Observations

Infrared data of CB 17 were obtained from the *Spitzer* Science Center (SSC). CB 17 was observed on 2004 February 12 with the Infrared Array Camera (IRAC; AOR key 4912384; PI: C. Lawrence) and 2004 October 16 with the Multiband Imaging Photometer for *Spitzer* (MIPS; AOR key 12025088; PI: G. Rieke). The IRAC observations were taken in the high dynamic range mode, with an effective long-frame exposure time of $\sim 130 \text{ s}$. The MIPS observations covered a field of $\sim 15' \times 55'$, with an exposure time of $\sim 190 \text{ s}$ at $24 \mu\text{m}$, $\sim 80 \text{ s}$ at $70 \mu\text{m}$, and $\sim 20 \text{ s}$ at $160 \mu\text{m}$, respectively. The data were processed by the *Spitzer* Science Center using their standard pipeline (version S18.7 for IRAC data and version S16.1 for MIPS data) to produce Post-Basic Calibration Data (P-BCD) images. The *Spitzer* spatial resolution is about $2''$ at the IRAC bands, and about $6''$, $18''$, and $40''$ at the MIPS 24, 70, and $160 \mu\text{m}$ bands, respectively. The overall flux calibration, expressed in physical units of MJy sr^{-1} , is estimated by the SSC to be accurate to within 10%. Table 2 lists the imaging sensitivity (1σ) of the IRAC and MIPS bands for CB17. For comparison, the imaging sensitivity for dark cloud L1448 (c2d data; Evans et al. 2003; 2009) is also listed. The *Spitzer* data of CB 17 have been already published by Launhardt et al. (2010).

3. RESULTS

3.1. Millimeter and Infrared Continuum Emission

Figure 1 shows the SMA 1.3 mm dust continuum image of CB 17, in which a centrally-peaked continuum source is clearly detected in the northwest of the SMA field of view. This continuum source is spatially associated with the infrared source IRS found by Launhardt et al. (2010), which dominates the infrared emission in the *Spitzer* images (see Figure 2) and is referred to as CB 17 IRS here. Located at the center of the SMA image, another faint continuum source is marginally detected (peak value $\sim 6\sigma$; see Figure 1), at an angular distance of $\sim 21''$ to the southeast of CB 17 IRS. This faint continuum source was independently detected in both the 2008 LSB ($\sim 5\text{--}6\sigma$) and 2009 LSB ($\sim 4\text{--}5\sigma$; depending on the cleaning-box and *uv*-weighting adopted in the data reduction) observations, but is not seen in the 2008 and 2009 USB observations. However, it must be noted that in our SMA observations the noises found in the USB are relatively higher than those in the LSB. This is evidenced by the observations of source CB 17 IRS, which was detected with the signal-to-noise ratios of ~ 8 and ~ 5 in the 2008 LSB ($1\sigma \sim 0.74 \text{ mJy beam}^{-1}$) and 2009 LSB ($1\sigma \sim 0.65 \text{ mJy beam}^{-1}$) observations, respectively, but only ~ 5 and ≤ 3 in the 2008 USB ($1\sigma \sim 0.85 \text{ mJy beam}^{-1}$) and 2009 USB ($1\sigma \sim 0.80 \text{ mJy beam}^{-1}$) observations. Therefore, the faint continuum source found in the LSB observations is likely missing in the USB observations due to the relatively lower single-to-noise ratio.

In the *Spitzer* images shown in Figure 2, this faint dust continuum source is located at the center of a small-scale dark shadow seen in the IRAC $8.0\mu\text{m}$ image (see Figure 2a), and no compact infrared emission is detected from this source at the *Spitzer* bands from 3.6 to $70\mu\text{m}$ (see Figure 2), although the MIPS $160\mu\text{m}$ map (spatial resolution $\sim 40''$) shows a slight shift of the peak position from the northwestern IRS source toward this faint source. Hereafter, we refer to the central faint continuum source as CB 17 MMS. We also note that CB 17 MMS is spatially associated with a faint infrared source detected in the *Herschel* PACS $100\mu\text{m}$ observations² (M. Schmalzl et al., in preparation; see Figure 2b) and a core detected in various high-density molecular line tracers in CB 17 (e.g., N_2H^+ and HCO^+ ; see Figure 2c). On the other hand, the IRAM-30m 1.3 mm dust continuum observations show two sub-cores with $\sim 14''$ separation in CB 17, named SMM1 and SMM2 (see Launhardt et al. 2010 and also Figure 2d). Interestingly, in the high angular resolution SMA images, no continuum source is detected within the sub-core SMM2, while the SMA 1.3 mm continuum source CB 17 MMS is

²There is an offset ($\sim 2''$) between the peaks of source CB 17 MMS and the faint infrared source seen at PACS $100\mu\text{m}$ (see Figure 2b). This offset is smaller than the SMA synthesized beam size ($\sim 3''$) and the PACS angular resolution at $100\mu\text{m}$ ($\sim 7''$), and is therefore not significant.

close to the sub-core SMM1, but $\sim 7''$ to the west of the peak position of the SMM1 core (see Figure 2d). This offset is larger than the pointing uncertainty in the IRAM-30m observations ($\sim 3''$ – $5''$). It is possible that the IRAM-30m single-dish observations detect the large-scale extended envelope, while the SMA observations reveal the relatively compact source which is embedded in this envelope, but not at its center.

Figure 3 shows the plots of the SMA visibility amplitudes versus uv distances for the continuum sources CB17IRS and MMS. As shown in the plots, CB17IRS shows a roughly flat distribution of amplitudes from long to short baselines, suggesting a compact, point-like object. For CB17MMS, the distribution also shows a roughly flat distribution at baselines longer than ~ 15 k λ ; at shorter baselines, the extended emission is mostly resolved (see below), and it is unclear if there is an Gaussian-like distribution, which is frequently seen in the interferometric observations toward protostellar envelopes (see, e.g., Looney et al. 2003). The SMA 1.3 mm continuum fluxes of sources CB17IRS and MMS were derived from Gaussian fitting of the restored images using the Miriad command *imfit* (see Table 3). For comparison, their fluxes integrated above the 3σ level are also listed. For source CB17IRS, its flux detected at SMA is ~ 6.3 mJy, roughly 20% of the flux found in the IRAM-30m image, where the flux density on its position is about ~ 30 mJy. For source CB17MMS, its flux derived from the SMA images is ~ 3.8 mJy, while its flux detected in the IRAM-30m 1.3 mm map is ~ 50 mJy (within the central $12''$ or 3000 AU of CB17MMS), indicating that more than 90% of the flux around CB17MMS was resolved out by the SMA.

Assuming that the 1.3 mm dust continuum emission is optically thin, the total gas mass (M_{gas}) is derived from the flux densities using the formula:

$$M_{\text{gas}} = \frac{F_{\nu} D^2}{\kappa_{\text{m}}(\nu) B_{\nu}(T_{\text{d}})} \left(\frac{M_{\text{g}}}{M_{\text{d}}} \right) \quad (1)$$

where D is the distance to the source, T_{d} is the dust temperature, $\kappa_{\text{m}}(\nu)$ is the dust opacity (mass absorption coefficient per gram of dust), and $M_{\text{g}}/M_{\text{d}}$ is the gas-to-dust mass ratio. Following Ossenkopf & Henning (1994), we adopt $\kappa_{\text{m}} = 0.5 \text{ cm}^2 \text{ g}^{-1}$, which is a typical value for dense cores with an average number density of $n(\text{H}) = 10^5 \text{ cm}^{-3}$. A standard gas-to-dust mass ratio of 150 is used, which is a combination of the ratio of Hydrogen mass to dust mass of 110 (Draine & Lee 1984) and the inclusion of Helium and heavier elements which introduces an extra factor of 1.36. A dust temperature of ~ 10 K was adopted for CB17MMS, which is derived from a fit to the SED (see below and also Launhardt et al. 2010) and is also similar to the mean kinetic gas temperature found in CB17 (see § 1). For CB17IRS, a dust temperature of ~ 20 K is adopted (see below). The relative uncertainties of the derived masses due to the calibration errors of the fluxes are within $\pm 20\%$. The

total gas masses of CB 17 MMS and IRS derived from the SMA observations are ~ 0.035 and $\sim 0.023 M_{\odot}$, respectively.

3.2. CO (2–1) Emission

Figure 4 shows the velocity channel maps of the SMA ^{12}CO (2–1) emission. The ^{12}CO emission is detected from $V_{\text{LSR}} = -7.2 \text{ km s}^{-1}$ to -2.2 km s^{-1} , with the cloud systematic velocity being $\sim -4.7 \text{ km s}^{-1}$ (Pavlyuchenkov et al. 2006). In each panel, the two crosses indicate the SMA positions of sources CB 17 IRS and MMS. In the CB 17 core, the observed FWHM of the optically thin N_2H^+ line is in the range of $0.25\text{--}0.45 \text{ km s}^{-1}$ (e.g., Benson et al. 1998), and we can safely assume that the (turbulent) CO cloud emission is within a velocity width of $\sim 2 \text{ km s}^{-1}$ (~ 5 times larger than the FWHM of N_2H^+). The ^{12}CO emission at velocities more than 1 km s^{-1} away from the cloud systematic velocity suggests the existence of molecular outflows in this region (see § 4.2 for more discussions, and Arce et al. 2010 for a discussion on differentiating between outflows and turbulence-related features). For CB 17 IRS, blueshifted emission (from $V_{\text{LSR}} = \sim -7.2 \text{ km s}^{-1}$ to $\sim -5.7 \text{ km s}^{-1}$) extends to the southeast, while redshifted emission (from $\sim -3.7 \text{ km s}^{-1}$ to $\sim -2.7 \text{ km s}^{-1}$) mainly extends to the northwest of the source. Near CB 17 MMS, blueshifted emission (from $V_{\text{LSR}} = \sim -7.2 \text{ km s}^{-1}$ to $\sim -5.7 \text{ km s}^{-1}$) extends to the east of the source, while redshifted emission (from $\sim -3.7 \text{ km s}^{-1}$ to $\sim -2.2 \text{ km s}^{-1}$) extends to both the west and east directions.

Figure 5 shows the velocity channel maps of the ^{13}CO (2–1) emission of CB 17, which is detected at velocities between ~ -5.2 and $\sim -4.2 \text{ km s}^{-1}$. The ^{13}CO (2–1) line emission associated with CB 17 IRS shows a circular centrally-peaked condensation coincident with the dust continuum source, while the emission near CB 17 MMS extends in both the west and east directions, similar to the morphology of the ^{12}CO (2–1) line emission. We also note that faint C^{18}O (2–1) emission is seen at the position of CB 17 IRS (see the spectrum in Figure 6), which shows a morphology similar to the ^{13}CO (2–1) emission (see Figure 7), while no C^{18}O (2–1) emission is detected from source CB 17 MMS in our SMA observations.

3.3. N_2D^+ (3–2) Emission

The N_2D^+ (3–2) line emission is also detected in the CB 17 observations. Figure 7 shows the velocity-integrated intensity map of the N_2D^+ (3–2) emission, plotted on the IRAC $8.0 \mu\text{m}$ image. The N_2D^+ (3–2) emission shows an elongated structure, which extends roughly in the east-west direction, and is spatially coincident with the dark shadow seen in the IRAC

8.0 μm image. The FWHM diameter of the N_2D^+ (3–2) condensation is measured to be $16.6'' \times 6.3''$ or 4200×1600 AU (at a distance of ~ 250 pc). Therefore, the condensation is resolved, as each axis is larger than the synthesized beam for N_2D^+ ($3.0'' \times 2.8''$). The HFS (HyperFine Structure) fitting routine in CLASS³, with the frequencies and weights adopted from Dore et al. (2004), was used to derive LSR velocity (V_{LSR}), line width (ΔV), optical depth (τ), and excitation temperature (T_{ex}). The optical depth (τ) is found to be small in most regions (ranging from 0.1 to 10, with typical values of 1–2). Hence, the N_2D^+ emission can be considered approximately optically thin, and the estimated excitation temperature is about 5–7 K. The measured integrated intensity of the N_2D^+ (3–2) emission is about $5 \text{ Jy beam}^{-1} \text{ km s}^{-1}$ or $\sim 14 \text{ K km s}^{-1}$. With the same method described in Caselli et al. (2002b), the column density of N_2D^+ is estimated to be $\sim 2\text{--}6 \times 10^{11} \text{ cm}^{-2}$.

The integrated intensity map of the C^{18}O (2–1) emission is also shown in Figure 7. Interestingly, the comparison between the N_2D^+ (3–2), C^{18}O (2–1), and 8.0 μm images suggests that N_2D^+ (3–2) traces only cold gas around source CB 17 MMS, while C^{18}O (2–1) traces relatively warm gas around infrared source CB 17 IRS. Furthermore, no strong N_2D^+ (3–2) emission is detected at the position of CB 17 MMS, but instead the N_2D^+ (3–2) emission shows a small arc-like structure surrounding the MMS source. It could be that N_2D^+ at the CB 17 MMS position has been destroyed by the gradually warming gas/dust due to the accreting luminosity of source CB 17 MMS.

Figure 8 shows the velocity field of CB 17, using the SMA N_2D^+ (3–2) data and derived with the same method described in Chen et al. (2007). The mean velocity map shows a continuous velocity gradient across the N_2D^+ condensation, increasing from southeast to northwest (see Figure 8a). A least-squares fitting of the velocity field indicates there is a velocity gradient of $18 \pm 1 \text{ km s}^{-1} \text{ pc}^{-1}$, with a position angle of $\sim -30^\circ$ (measured east of north in the direction of increasing velocity), in the core traced by the N_2D^+ emission.

The line widths are roughly constant within the condensation (with a typical value of $\sim 0.5 \text{ km s}^{-1}$) and relatively large line widths ($1.0\text{--}1.2 \text{ km s}^{-1}$) are mainly seen at the south-east southeast edge (see Figure 8b). We note that the velocity resolution in the N_2D^+ observations is $\sim 0.25 \text{ km s}^{-1}$. Therefore, the typical line width of 0.5 km s^{-1} derived in the observations can be considered as an upper limit (given higher velocity resolution observations, we may expect to find narrower line widths between $0.25\text{--}0.50 \text{ km s}^{-1}$). Assuming a kinetic gas temperature of 10 K (see § 1), the thermal contribution to the N_2D^+ line width is $\sim 0.13 \text{ km s}^{-1}$, and the typical non-thermal contribution to the line width is then $\sim 0.48 \text{ km s}^{-1}$, which is about 3.7 times larger than the thermal line width. Although the ori-

³see <http://www.iram.fr/IRAMFR/GILDAS>

gin of the non-thermal line width is still a subject of an ongoing debate, it is widely accepted that turbulence is the main contributor (see, e.g., Goodman et al. 1998). On the other hand, the thermal FWHM line width of an “average” particle of mass $2.33 m_{\text{H}}$ (assuming gas with 90% H_2 and 10% He), which represents the local sound speed, would be $\sim 0.44 \text{ km s}^{-1}$ at 10 K. The observed non-thermal line width in N_2D^+ is comparable with this value, which suggests that turbulence in the condensation is approximately sonic.

4. DISCUSSION

4.1. Spectral Energy Distributions

Figure 9 shows the spectral energy distribution of CB 17 IRS. The submillimeter and millimeter fluxes of CB 17 IRS were estimated from the SCUBA and IRAM-30m dust continuum images (see Launhardt et al. 2010). The fluxes in the *Spitzer* images were measured with aperture photometry in the IRAF APPHOT package, with the radii, background annuli, and aperture corrections recommended by the *Spitzer* Science Center. We note that CB 17 is actually associated with a faint and cold IRAS point source (IRAS 04005+5647, $F_{100\mu\text{m}} = 5.78 \text{ Jy}$, $F_{60\mu\text{m}} = 0.91 \text{ Jy}$, not detected at shorter wavelengths). Given that no compact infrared emission was detected from CB 17 MMS in the *Spitzer* 3.6–70 μm images but CB 17 IRS was detected at these bands, we assume that all the IRAS flux comes from CB 17 IRS⁴. Table 4 lists all the flux points of CB 17 IRS plotted in Figure 9. To derive luminosities and temperatures, we first interpolated and then integrated the SED, always assuming spherical symmetry. Interpolation between the flux densities was done by a χ^2 single-temperature grey-body fit to all points (including upper limits) at $\lambda \geq 100 \mu\text{m}$, using the same method as described in Chen et al. (2008). A simple logarithmic interpolation was performed between all points at $\lambda < 100 \mu\text{m}$. The results from the SED fitting of CB 17 IRS, such as $T_{\text{bol}} \sim 50 \text{ K}$, $T_{\text{dust}} \sim 20 \text{ K}$, and $L_{\text{smm}}/L_{\text{bol}} \sim 2\%$, in concert with the fact that it is directly observed in the near-infrared wavelengths (see Launhardt et al. 2010), suggest that CB 17 IRS is a Class 0/I transition object with a luminosity of $L_{\text{bol}} \sim 0.5 L_{\odot}$.

For comparison, we also show in Figure 9 the SED of source CB 17 MMS. The mm and submm fluxes of CB 17 MMS were estimated using the IRAM-30m and SCUBA dust continuum images (see Launhardt et al. 2010). The flux within one beam of CB 17 MMS

⁴This is also consistent with the infrared observations taken with the *Herschel Space Observatory* (M. Schmalzl et al. in preparation). In the *Herschel* PACS observations at $100\mu\text{m}$, source CB 17 IRS dominates the infrared emission (see Figure 2b), with a flux ratio of more than 30 compared to source CB 17 MMS.

is ~ 50 mJy at 1.3 mm, ~ 180 mJy at $850\ \mu\text{m}$, and < 800 mJy at $450\ \mu\text{m}$ (3σ upper limit, no detection). Although the MIPS3 image at $160\ \mu\text{m}$ does not resolve sources CB17 IRS and MMS, a slight shift of the peak position from IRS toward MMS suggests detectable emission from MMS at this wavelength (see Figure 2d). For compiling the SED, we assigned 15% of the total $160\ \mu\text{m}$ flux to MMS (see also Launhardt et al. 2010), but our results depend only weakly on the adopted flux splitting. Table 4 lists all the flux points and upper limits of CB17 MMS. The estimated bolometric luminosity of CB17 MMS is less than $0.04\ L_{\odot}$, and the dust temperature derived from the SED fit is ~ 10 K.

The fact that no infrared emission was detected from CB17 MMS in the *Spitzer* 3.6– $70\ \mu\text{m}$ images suggests this source is extremely cold; the estimated bolometric temperature of the source is about 16 K. We note that the imaging sensitivity of the CB17 *Spitzer* data is about 1.5 times deeper than that obtained by the c2d observations of other cores (see Table 2 for a comparison). Given that the c2d data are sensitive to embedded protostars with internal luminosity⁵ $L_{\text{int}} \leq 4 \times 10^{-3} (d/140\text{ pc})^2 L_{\odot}$ (see Dunham et al. 2008), the internal luminosity of a potential protostar in CB17 MMS should be less than $0.013\ L_{\odot}$ at a distance of 250 pc, which is consistent with the upper limit of the bolometric luminosity obtained from our SED fitting ($\sim 0.04\ L_{\odot}$). Nevertheless, it must be noted that uncertainties remain in our estimates, due to the limited observations available. More observations, such as high angular resolution and high sensitivity continuum observations at wavelengths from far-infrared to (sub-)millimeter, are needed to constrain the SED of CB17 MMS in order to derive more precisely its luminosity and temperature.

4.2. Outflows in CB 17

Figure 10 shows the velocity-integrated intensity map of the SMA ^{12}CO (2–1) emission of CB 17, plotted on the IRAC $8.0\ \mu\text{m}$ image. For source CB17 IRS, its CO emission shows a typical bipolar morphology seen in low-mass protostellar outflows (see, e.g., Arce & Sargent 2006; Jørgensen et al. 2007). From the SMA data, we estimate the opening angle of the blue lobe to be ~ 85 degrees and the position angle (measured east from north) is ~ 125 degrees. The outflow’s inclination (with respect to the plane of the sky) is estimated to be ~ 50 degrees, using geometrical case 4 in Cabrit & Bertout (1986). Near source CB17 MMS, the blueshifted and redshifted emissions show long and narrow structures (~ 7500 AU and ~ 8500 AU in length, respectively), extending in the east-west direction and overlapping

⁵The internal luminosity is the luminosity of the central source, which excludes the luminosity arising from external heating.

each other, different from the morphology of the bipolar outflow associated with source CB 17 IRS. Because CB 17 MMS is such an extremely low luminosity object, we discuss below five possible mechanisms that might produce the observed CO emission around CB 17 MMS.

Firstly, the CO lobes around CB 17 MMS might be artifacts due to incomplete uv -coverage in the interferometric observations. However, the CO emission around CB 17 MMS is strong, and shows consistent velocity structure and morphology, which do not change significantly with data reduction methods (e.g., various uv weighting, velocity resolution, and clean method adopted). More importantly, our observations taken in 2008 (eight antennas, 6.5 hours integration time) and 2009 (seven antennas, 3.3 hours integration time) produce the same velocity structure and morphology around CB 17 MMS, indicating that these CO structures are independent of the uv sampling. Therefore, we consider these CO lobes around CB 17 MMS are not artifacts in the interferometric maps.

Secondly, the low velocity ($\sim 2.5 \text{ km s}^{-1}$) CO line emission might suggest that the emission could be due to bound motions in the cloud core. However, for gas at 2 km s^{-1} to be bound to the core at a distance of 7500 AU (measured using the blue lobe), it would require a core mass of $\sim 17 M_{\odot}$, which is much larger than the core mass derived from the IRAM-30m continuum observations ($\sim 4 M_{\odot}$, radius 8000 AU; Launhardt et al. 2010) and the virial mass derived from molecular line observations ($\sim 3 M_{\odot}$, e.g., Caselli et al. 2002a; scaled to the radius of 7500 AU). This indicates that the CO emission is not from spurious structures of the cloud core.

The third possibility is that the two long and narrow CO lobes around CB 17 MMS are caused by the outflow from CB 17 IRS, which impacts and deflects from the dense region near CB 17 MMS. However, (1) the geometry of the system is not quite consistent with this picture. As seen in Figure 10, the redshifted outflow of CB 17 IRS mainly extends to the northwest, but the red lobe around CB 17 MMS mainly extends to the east. (2) The outflow from CB 17 IRS is much weaker than the elongated lobes close to CB 17 MMS (see Table 5). The velocity-integrated intensity of the CO emission from the two lobes around CB 17 MMS (~ 19.5 and $\sim 23.3 \text{ Jy beam}^{-1} \text{ km s}^{-1}$ for the blue and red lobes, respectively) is much larger than that of the two lobes in the CB 17 IRS outflow (~ 16.9 and $\sim 14.2 \text{ Jy beam}^{-1} \text{ km s}^{-1}$ for the blue and red lobes, respectively). We believe that it is unlikely for a weak outflow, like that of CB 17 IRS, to produce a much stronger outflow as a result from its deflection from a dense core. And (3), if the CO emission around source CB 17 MMS is impacted and deflected from the CB 17 IRS outflow, we might expect to find intense turbulence around CB 17 MMS, but in contrast, the dense core around CB 17 MMS is very quiescent, as indicated by the narrow linewidth in the optically thin N_2H^+ observations (see Bensen et al. 1998; Caselli et al. 2002a) and N_2D^+ observations (this work).

The fourth possibility is that the CO lobes around CB 17 MMS are actually parts of the outflow lobes of CB 17 IRS, and these features could result from missing flux in the interferometric observations. However, the geometry of the system is not consistent with this picture. As we discussed above, the redshifted outflow of CB 17 IRS mainly extends to the northwest, but the red lobe around CB 17 MMS mainly extends to the east. Therefore, even if we assumed that the blue lobe around CB 17 MMS is part of the blueshifted outflow driven by CB 17 IRS, it would be difficult to explain the existence of the red lobe to the east of CB 17 MMS.

Finally, the fifth possibility is that the two CO lobes around source CB 17 MMS represent the molecular outflow driven by CB 17 MMS. The peculiar morphology (i.e., blue and red outflow lobes are overlapping) and the low radial velocity of the gas suggest that these blue- and redshifted lobes may be produced by a collimated outflow with an axis close to the plane of the sky, similar to the RNO 43 outflow (e.g., Arce & Sargent 2005; see also Figure 1 of Cabrit et al. 1988 for a diagram of the geometry of an outflow close to the plane of the sky). If this is the case, then it is probable that we do not detect higher velocities CO emission due to projection effects (we return to this point in § 4.3.2). We consider this the most likely scenario, and hereafter we assume the observed narrow ^{12}CO structures are associated with a molecular outflow driven by CB 17 MMS. Nevertheless, we note that further observations (e.g., SMA subcompact data) are needed to recover the missing flux of the extended structure, and to confirm the nature of these narrow ^{12}CO structures.

Since the ^{13}CO (2–1) emission from CB 17 MMS is detected only at velocities between ~ -5 and $\sim -4 \text{ km s}^{-1}$ (see Figure 5), we may consider that the ^{12}CO (2–1) emission at velocities beyond this range to be optically thin. The outflow masses of the two sources are derived with the same method as described in Cabrit & Bertout (1990; 1992). In the calculations, we assume LTE conditions and an excitation temperature of 20 K. The derived outflow mass, as well as other outflow properties (e.g., momentum P and energy E), are listed in Table 5. The outflow mass-loss rate (\dot{M}_{out}), force (F_{m}), and mechanical luminosity (L_{m}) are estimated from the mass, momentum, and energy with the estimated dynamical age of the outflow. For the CB 17 MMS outflow, assuming that the outflow velocity is 2.5 km s^{-1} , the dynamical age of the outflow is estimated to be $\sim 1.4 \times 10^4 \text{ yr}$ (the inclination effect is not considered here). For the CB 17 IRS outflow, assuming the same outflow velocity and an inclination angle of ~ 50 degrees, the dynamical age of the outflow is estimated to be $\sim 1.1 \times 10^4 \text{ yr}$. We note that these outflow parameters in Table 5 refer only to the compact outflows detected in the SMA maps and thus represent lower limits only.

4.3. The Nature of CB 17 MMS

4.3.1. Comparisons to prestellar and Class 0 objects

Although the SMA and *Spitzer* observations clearly indicate that source CB 17 IRS is a Class 0/I transition object, the evolutionary stage of source CB 17 MMS is unclear. Previous single-dish molecular line observations have shown subsonic infall ($\sim 0.05 \text{ km s}^{-1}$), slow rotation ($\sim 2 \text{ km s}^{-1} \text{ pc}^{-1}$), and subsonic internal turbulent ($\sim 0.1 \text{ km s}^{-1}$) motions in the CB 17 dense core (see Pavlyuchenkov et al. 2006), which are similar to the typical properties found in prestellar cores (see, e.g., André et al. 2009). These early results of CB 17⁶, in concert with the fact that no compact infrared emission is detected from CB 17 MMS in the *Spitzer* images, led to the idea that CB 17 MMS may be a prestellar core (e.g., Launhardt et al. 2010). However, the SMA 1.3 mm dust continuum observations suggest that a compact object has formed in CB 17 MMS. In contrast, prestellar cores generally show no compact dust continuum emission in high angular resolution interferometric observations (e.g., Olmi et al. 2005; Schnee et al. 2010; but see also Bourke et al. 2012). Furthermore, the SMA CO (2–1) observations suggest that CB 17 MMS drives a molecular outflow, which implies active accretion/ejection motions in source CB 17 MMS — unlikely to take place in a prestellar core. Moreover, Pavlyuchenkov et al. (2006) suggested that the CB 17 core is chemically evolved, with an age of $\sim 2 \text{ Myr}$, which is somewhat larger than the typical lifetimes of prestellar cores ($\sim 1\text{--}1.5 \times 10^6 \text{ yr}$; see André et al. 2009).

On the other hand, compared to the typical properties of Class 0 protostars, CB 17 MMS shows also three major differences. Firstly, CB 17 MMS is not visible in the deep *Spitzer* images at wavelengths from 3.6 to $70 \mu\text{m}$, with an extremely low bolometric luminosity ($\leq 0.04 L_{\odot}$), which implies no central protostellar object formed yet within the dense core. For comparison, most Class 0 protostars, if not all, are detectable in the *Spitzer* infrared images (at least in the MIPS bands; see, e.g., Evans et al. 2009). Secondly, the SMA 1.3 mm dust continuum observations suggest the existence of a compact, but very faint, object in CB 17 MMS (see § 3.1). The mm continuum flux of CB 17 MMS (only a few mJy) is about two magnitudes lower than the values of those Class 0 protostars observed with the same configuration at the SMA (generally in the order of $\sim 100 \text{ mJy}$ or $\sim 0.1 M_{\odot}$; see, e.g., Jørgensen et al. 2007), implying that no massive accretion disk has developed yet around CB 17 MMS. Lastly, CB 17 MMS appears to drive a relatively slow molecular outflow ($\sim 2.5 \text{ km s}^{-1}$), compared to those typically found in Class 0 protostars, which have velocities

⁶The previous single-dish line observations toward CB 17 generally show a dense core centered at the position of source CB 17 MMS. Therefore, we consider that the properties derived from these single-dish line observations are related to source MMS rather than source IRS.

of ~ 10 to 100 km s^{-1} and have strong (physical and chemical) impacts on their surrounding cores and clouds (see, e.g., Arce et al. 2007).

From the comparisons discussed above, we suggest that source CB17MMS is more evolved than prestellar cores but less evolved than Class0 protostars, as it preserves many typical properties of prestellar cores seen in the early single-dish observations (i.e., in the outer core), but it also shows properties (e.g., compact object and outflow) that only protostars exhibit, in the high angular resolution observations (i.e., in the inner core), though neither strong protostellar object nor massive accretion disk appear to have developed yet in it.

4.3.2. A Candidate First Hydrostatic Core?

Interestingly, the observed properties of CB17MMS are consistent with the theoretical predictions of the radiative hydrodynamical (RHD) simulations for the first hydrostatic core (or first core), a transient object intermediate between the prestellar and Class0 phases (see, e.g., Larson 1969; Masunaga et al. 1998). Theoretical studies have investigated the properties of the first core and made a series of observationally testable predictions, including a short lifetime of only 10^3 – 10^4 years, an extremely low bolometric luminosity ($< 0.1 L_\odot$), very low mass ($< 0.1 M_\odot$), and no detectable infrared emission at wavelengths shorter than $30 \mu\text{m}$ (see, e.g., Boss & Yorke 1995; Masunaga et al. 1998; Machida et al. 2008). In Figure 11, we compare the fluxes of source CB17MMS with those of a first hydrostatic core modeled by Masunaga et al. (1998). Although the number of observational data points is still small, the comparisons show that the fluxes of CB17MMS are in general agreement with those of a first hydrostatic core calculated with a beam size of 1000 AU (or $4''$ at the distance of CB17), which would have a luminosity of $\sim 0.06 L_\odot$ when the core central density reaches $\rho_{\text{center}} \sim 10^{-9} \text{ g cm}^{-3}$ or evolves at $\sim 1.23 \times$ free-fall time (model M1a; see Masunaga et al. 1998 for more details).

In addition, the radius of the first core is found to be small, typically $\sim 5 \text{ AU}$ (Masunaga et al. 1998). When the effects of rotation are considered, this radius can be a little larger, in the range of 10–20 AU (Saigo & Tomisaka 2006; Saigo et al. 2008). Generally, in the interferometric dust continuum observations, prestellar cores show no compact dust continuum emission (i.e. no detection) with existing millimeter interferometers (e.g., Olmi et al. 2005; Schnee et al. 2010; Offner et al. 2012; X. Chen et al. in preparation), because the extended structure of prestellar core (typically with density of $\rho \sim 10^{-19} \text{ g cm}^{-3}$, or ~ 10 magnitudes smaller than that of the first core) will be almost totally resolved out by millimeter interferometric observations. While a core evolves from prestellar core to the onset of the first core,

we expect to find a relatively compact, point-like, but also faint (≤ 50 mJy, judged from the models in Masunaga et al. 1998) object in the interferometer observations. As can be seen in Figure 3, the SMA visibility amplitudes versus uv distances diagram of CB 17 MMS shows a roughly flat distribution, which suggests a point-like object in CB 17 MMS with a flux of ~ 3 mJy, consistent with the prediction of the small radius and small flux of the first core. However, we note that the SMA compact configuration observations mainly sample the uv range between ~ 10 – 60 k λ . Further subcompact and extended configurations are definitely needed to study in detail the density structure of CB 17 MMS.

Moreover, the SMA CO (2–1) observations suggest that CB 17 MMS drives a molecular outflow. Interestingly, recent MHD simulations have shown that the first cores can drive low-velocity outflows (see, e.g., Machida et al. 2008; Tomida et al. 2010). In the simulations, the typical outflow driven by a first core has velocities of ~ 2 – 5 km s $^{-1}$ (e.g., Machida et al. 2008). The observed velocity of the CB 17 MMS outflow is about 2.5 km s $^{-1}$, which is in good agreement with the result from the MHD simulations. However, in the MHD simulations (e.g., Machida et al. 2008), the outflow driven by the first core also features wide opening-angle and low extent-to-width (E/W) ratio (2.2 – 2.5)⁷. The outflow driven by CB 17 MMS shows two narrow lobes, overlapping with each other, with opening angle of $\sim 35^\circ$ and E/W of ~ 4 (measured using the blue lobe), which is more consistent with a protostellar outflow rather than a first core outflow. However, it must be noted that the opening-angle and E/W measured in the CB 17 MMS outflow are best treated as upper limits, because the SMA compact configuration observations recover only the fluxes at projected baselines > 10 k λ (corresponding to angular scales $< 20''$). Further short-spacing observations are needed to recover the extended structure of the CB 17 MMS outflow, in order to derive more precisely its opening-angle and E/W ratio. In MHD simulations, both magnetic field and rotation rate in the collapsing core shape the morphology of the first core outflow (see, e.g., Machida et al. 2008). Hence, there is also the possibility that the CB 17 MMS outflow represent a first core outflow that results from a specific magnetic field and/or rotation rate.

Another significant unknown factor in our analysis of the CB 17 MMS outflow is the source inclination. With the SMA CO images of CB 17 MMS, we are unable to set strong constraints on the inclination from the outflow morphology, although the extreme face-on ($\leq 10^\circ$) configuration can be ruled out here. If CB 17 MMS is viewed along a relatively edge-on line-of-sight ($> 60^\circ$), the true velocity of the outflow would increase beyond the outflow velocity expected for the first core. For example, an inclination of 80° would increase the outflow velocity from the observed value of 2.5 to 14 km s $^{-1}$. On the other hand, if we assumed

⁷More recently, smoothed particle magneto-hydrodynamics simulations suggest that the first hydrostatic core can drive collimated jets (opening angles $\leq 10^\circ$) with speeds of ~ 2 – 7 km s $^{-1}$ (see Price et al. 2012).

an inclination of 45° , the outflow velocity of CB 17 MMS would be about 3.5 km s^{-1} , which is still comparable with the predicted values of the first core outflows (but in this case, the extent-to-width ratio would increase to ~ 6). Furthermore, source inclination also has strong effects on the observed infrared properties. For a protostar surrounded by a circumstellar disk and embedded in a dense envelope, the infrared emission would be much stronger when viewed near face-on where the emission can escape through outflow cavities, than when viewed near edge-on where the emission is reprocessed by the disk and dense inner envelope. Clearly, better knowledge of the source inclination would help in determining the true evolutionary status of CB 17 MMS.

At present, unfortunately, due to the insufficient observations and uncertain inclination angle, the nature of source CB 17 MMS is still not definitive. With the combined results from early single-dish observations and our SMA and *Spitzer* observations, in concert with the comparisons to theoretical models, we consider that CB 17 MMS may represent a candidate first hydrostatic core. Nevertheless, there is also the possibility that CB 17 MMS is an extremely low luminosity protostar, which is deeply embedded in an *edge-on* circumstellar disk/inner envelope and thus shows no detectable infrared emission in the deep *Spitzer* observations.

4.3.3. Comparisons with other first core candidates

The detection of the first hydrostatic core phase is of prime importance in our understanding of the early evolution of dense cores and the origin of outflows, as it would not only confirm the long prediction of RHD models but also set strong constraints on MHD models of protostellar outflows. On the observational side, the search for the first core has been going on for a while and several first core candidates have been proposed, although none of them have been verified. Based on the SMA and *Spitzer* observations, we reported a first core candidate, L1448 IRS 2E, which is invisible in the sensitive *Spitzer* infrared images (from 3.6 to $70 \mu\text{m}$), has very weak (sub-) millimeter dust continuum emission, and consequently has an extremely low luminosity ($L_{\text{bol}} < 0.1 L_\odot$), but also drives a molecular outflow (Chen et al. 2010). Enoch et al. (2010) reported another candidate first core, Per-Bolo 58, a very low luminosity (internal luminosity $< 0.01 L_\odot$) dense core in Perseus. This core was originally thought to be starless, but Enoch et al. (2010) detected an associated infrared source in very deep *Spitzer* $24 \mu\text{m}$ and $70 \mu\text{m}$ observations and argued this source could either be a first core or a very low luminosity Class 0 protostar. A bipolar, jet-like molecular outflow was also found in this interesting source by Dunham et al. (2011). More recently, Pineda et al. (2011) reported another candidate, L1451-mm, which is not visible in the

Spitzer observations (with a bolometric luminosity of $< 0.05 L_{\odot}$) and drives a low-velocity, poorly-collimated, bipolar outflow.

Together with CB17 MMS, these sources are all suggested candidates of the long predicted first hydrostatic core, but none of them are in complete agreement with theoretical models. For source L1448 IRS 2E, its outflow velocity reaches $\sim 25 \text{ km s}^{-1}$ (see Chen et al. 2010), much larger than the value predicted by the MHD simulations. In the case of Per-Bolo 58, its detection at $24 \mu\text{m}$ is inconsistent with current models. For source L1451-mm, its observations are in better agreement with theoretical models, but its SED and continuum interferometric visibilities can also be equally well fitted by a model of a protostar plus a circumstellar disk (see Pineda et al. 2011). For source CB17 MMS, another promising candidate, its outflow is much more collimated than that expected for a first core, and there is a possibility that it is an extremely low luminosity protostar deeply embedded in an edge-on circumstellar disk.

Clearly, more observations are needed to study these sources thoroughly: (1) high angular resolution and high sensitivity continuum observations at wavelengths from far-infrared to (sub-) millimeter, are needed to constrain the SEDs of these sources, in order to derive more precisely their luminosities and temperatures, and (2) high angular and spectral resolution line observations are also needed to study in detail the physical properties, density structure, kinematics, and chemistry of the surrounding dense gas around the sources in order to accurately characterize their evolutionary status. It is also critical to search for more candidate first cores in nearby clouds, in order to achieve a better understanding of the formation and evolution of dense cores, as well as the origin of outflows. With the availability of recent sensitive (sub-) millimeter telescopes (e.g., *Herschel Space Observatory* and the Atacama Large Millimeter/Submillimeter Array), we believe that more candidates will be found in the near future.

5. SUMMARY

We present SMA 230 GHz and *Spitzer* infrared observations toward the Bok globule CB17. The SMA 1.3 mm dust continuum images reveal within CB17 two sources, which are separated by $\sim 21''$ ($\sim 5250 \text{ AU}$) in the northwest-southeast direction. The northwestern continuum source, referred to as CB17 IRS (gas mass $\sim 0.023 M_{\odot}$), dominates the infrared emission in the *Spitzer* images and drives a low-velocity bipolar outflow detected in the SMA CO(2–1) observations. The SED fitting results suggest that CB17 IRS is a low luminosity Class 0/I transition object ($L_{\text{bol}} \sim 0.5 L_{\odot}$).

The southeastern continuum source, referred to as CB17 MMS, has faint dust continuum emission in the SMA 1.3 mm images ($\sim 6\sigma$ detection; gas mass $\sim 0.035 M_\odot$), and is not detected in the deep *Spitzer* images at wavelengths from $3.6 \mu\text{m}$ to $70 \mu\text{m}$. Its bolometric luminosity and temperature, estimated from the SED fitting, are $\leq 0.04 L_\odot$ and $\leq 16 \text{ K}$, respectively. The SMA N_2D^+ (3–2) observations show an elongated condensation associated with source CB17 MMS, which has a systematic velocity gradient of $18 \pm 1 \text{ km s}^{-1} \text{ pc}^{-1}$ and a typical line width of $\sim 0.48 \text{ km s}^{-1}$. Interestingly, the SMA CO (2–1) observations suggest that CB17 MMS may drive a long narrow low-velocity outflow ($\sim 2.5 \text{ km s}^{-1}$), with blueshifted and redshifted lobes extending in the east-west direction, that overlap each other. Comparisons with prestellar cores and Class 0 protostars suggest that CB17 MMS is likely at an evolutionary stage intermediate between these two stages. The observed characteristics of CB17 MMS are consistent with the properties expected for the first hydrostatic core as predicted by radiative/magneto hydrodynamical simulations. We thus consider CB17 MMS to be a candidate first core. However, there is also the possibility that CB17 MMS is an extremely low luminosity protostar, which is deeply embedded in an edge-on circumstellar disk/inner envelope. Further high angular resolution and high sensitivity observations are needed to confirm the properties of CB17 MMS and to address more precisely its evolutionary stage.

We thank the SMA staff for technical support during the observations and the *Spitzer* Science Center for their maintenance of the *Spitzer* data. This material is based on work supported by NSF grant AST-0845619 to H.G.A. This research is supported in part by the National Science Foundation under grant number 0708158 (T.L.B.).

REFERENCES

- André, P., Basu, S., & Inutsuka, S.-I. 2009, in *Structure Formation in Astrophysics*, ed. G. Chabrier (Cambridge: Cambridge University Press), 254
- André, P., Ward-Thompson, D., & Barsony, M. 2000, in *Protostars and Planets IV*, ed. V. Mannings, A. P. Boss, & S. S. Russell (Tucson: Univ. Arizona Press), 59
- Arce, H. G., Borkin, M. A., Goodman, A. A., Pineda, J. E., & Halle, M. W. 2010, *ApJ*, 715, 1170
- Arce, H. G., & Sargent, A. I. 2005, *ApJ*, 624, 232
- Arce, H. G., & Sargent, A. I. 2006, *ApJ*, 646, 1070
- Arce, H. G., Shepherd, D., Gueth, F., Lee, C.-F., & Bachiller, R., et al. 2007, in *Protostars and Planets V*, ed. B. Reipurth, D. Jewitt, & K. Keil (Tucson: Univ. Arizona Press), 245
- Benson, P. J., Caselli, P., & Myers, P. C. 1998, *ApJ*, 506, 743
- Boss, A. P., & Yorke, H. W. 1995, *ApJ*, 439, L55
- Bourke, T. L., Myers, P. C., Caselli, P., Di Francesco, J., Belloche, A. et al. 2012, *ApJ*, 745, 117
- Bourke, T. L., Myers, P. C., Evans II, N. J., Dunham, M. M., & Kauffmann, J., et al. 2006, *ApJ*, 649, L37
- Cabrit, S., & Bertout, C. 1986, *ApJ*, 307, 313
- Cabrit, S., & Bertout, C. 1990, *ApJ*, 348, 530
- Cabrit, S., & Bertout, C. 1992, *A&A*, 261, 276
- Cabrit, S., Goldsmith, P. F., & Snell, R. L. 1988, *ApJ*, 334, 196
- Caselli, P., Benson, P. J. Myers, P. C., & Tafalla, M. 2002a, *ApJ*, 572, 238
- Caselli, P., Walmsley, C. M., Zucconi, A., Tafalla, M., Dore, L., & Myers, P. C. 2002b, *ApJ*, 565, 344
- Chen, X., Arce, H. G., Zhang, Q., Bourke, T. L., & Launhardt, R., et al. 2010, *ApJ*, 715, 1344

- Chen, X., Launhardt, R., Bourke, T., Henning, Th., & Barnes, P. J. 2008, *ApJ*, 683, 862
- Chen, X., Launhardt, R., & Henning, Th. 2007, *ApJ*, 669, 1058
- Clemens, D. P., & Barainis, R. 1988, *ApJS*, 68, 257
- Dame, T. M., Ungerechts, H., Cohen, R. S., de Geus, E. J., & Grenier, I. A., et al. 1987, *ApJ*, 322, 706
- Di Francesco, J., Evans, N. J., Caselli, P., Myers, P. C., & Shirley, Y., et al. 2007, in *Protostars and Planets V*, ed. B. Reipurth, D. Jewitt, & K. Keil (Tucson: Univ. Arizona Press), 17
- Dore, L., Caselli, P., Beninati, S., Bourke, T., Myers, P. C., & Cazzoli, G. 2004, *A&A*, 413, 1177
- Draine, B. T., & Lee, H. M. 1984, *ApJ*, 285, 89
- Dunham, M. M., Chen, X., Arce, H. G., Bourke, T. L., Schnee, S., & Enoch, M. L. 2011, *ApJ*, 742, 1
- Dunham, M. M., Crapsi, A., Evans II, N. J., Bourke, T. L., & Huard, T. L., et al. 2008, *ApJS*, 179, 249
- Enoch, M. L., Lee, J.-E., Harvey, P., Dunham, M. M., & Schnee, S. 2010, *ApJ*, 722, L33
- Evans II, N. J., Allen, L. E., Blake, G. A., Boogert, A. C. A., & Bourke, T. L., et al. 2003, *PASP*, 115, 965
- Evans II, N. J., Dunham, M. M., Jørgensen, J. K., Enoch, M. L., & Merín, B., et al. 2009, *ApJS*, 181, 321
- Goodman, A. A., Barranco, J. A., Wilner, D. J., Heyer, M. H. 1998, *ApJ*, 504, 223
- Ho, P. T. P., Moran, J. M., & Lo, K. Y. 2004, *ApJ*, 616, L1
- Jørgensen, J. K., Bourke, T. L., Myers, P. C., Di Francesco, J., & van Dishoeck, E. F., et al. 2007, *ApJ*, 659, 479
- Kane, B. D., & Clemens, D. P. 1997, *AJ*, 113, 1799
- Larson, R. B. 1969, *MNRAS*, 145, 271
- Launhardt, R., Evans II, N. J., Wang, Y., Clemens, D. P., & Henning, Th., et al. 1998, *ApJS*, 119, 59

- Launhardt, R., Nutter, D., Ward-Thompson, D., Bourke, T. L., & Henning, Th., et al. 2010, *ApJS*, 188, 139
- Lemme, C. Wilso, T. L., Tieftrunk, A. R., & Henkel, C. 1996, *A&A*, 312, 585
- Lindblad, P. O., Grape, K., Sandqvist, A., & Schober, J. 1973, *A&A*, 24, 309
- Looney, L. W., Mundy, L. G., & Welch, W. J. 2003, *ApJ*, 592, 255
- Machida, M., Inutsuka, S.-I., & Matsumoto, T. 2008, *ApJ*, 676, 1088
- Masunaga, H., Miyama, S. M., & Inutsuka, S.-I. 1998, *ApJ*, 495, 346
- Offner, S. S. R., Capodilupo, J., Schnee, S., & Goodman, A. A. 2012, *MNRAS*, 420, L53
- Olmi, L., Testi, L., & Sargent, A. I. 2005, *A&A*, 431, 253
- Ossenkopf, V., & Henning, Th. 1994, *A&A*, 291, 943
- Pavlyuchenkov, Ya., Wiebe, D., Launhardt, R., & Henning, Th. 2006, *ApJ*, 645, 1212
- Pineda, J. E., Arce, H. G., Schnee, S., Goodman, A. A., & Bourke, T. L., et al. 2011, *ApJ*, 743, 201
- Price, D. J., Tricco, T. S., & Bate, M. R., 2012, *MNRAS*, in press (axXiv:1203.2933)
- Qi, C. 2005, *MIR Cookbook* (Cambridge: Harvard), <http://cfa-www.harvard.edu/~cqi/mircook.html>
- Reipurth, B., Jewitt, D., & Keil, K. 2007, ed., *Protostars and Planets V* (Univ. Arizona Press)
- Saigo, K., & Tomisaka, K. 2006, *ApJ*, 645, 381
- Saigo, K., Tomisaka, K., & Matsumoto, T. 2008, *ApJ*, 674, 997
- Sault, R. J., Teuben, P. J., & Wright, M. C. H. 1995, in *ASP Conf. Ser. 77, Astronomical Data Analysis Software and Systems IV*, ed. R. A. Shaw, H. E. Payne, & J. J. E. Hayes (San Francisco: ASP), 443
- Schnee, S., Enoch, M., Johnstone, D., Culverhouse, T., & Leitch, E., et al. 2010, *ApJ*, 718, 306
- Shu, F. H., Adams, F. C., & Lizano, S. 1987, *ARA&A*, 25, 23

- Tomida, K., Tomisaka, K., Matsumoto, T., Ohsuga, K., Machida, M. N., & Saigo, K. 2010, *ApJ*, 714, L58
- Turner, B. E., Herbst, E., & Terzieva, R. 2000, *ApJS*, 126, 427
- Turner, B. E., Pirogov, L., & Minh, Y. C. 1997, *ApJ*, 483, 235
- van Leeuwen, F., (e.d.) 2007, *Astrophysics and Space Science Library*, Vol. 350, *Hipparcos, the New Reduction of the Raw Data* (Dordrecht: Springer)
- Ward-Thompson, D., André, P., Crutcher, R., Johnstone, D., & Onishi, T., & Wilson, C. 2007, in *Protostars and Planets V*, ed. B. Reipurth, D. Jewitt, & K. Keil (Tucson: Univ. Arizona Press), 33
- Young, C. H., Jørgensen, J. K., Shirley, Y. L., Kauffmann, J., & Huard, T., et al. 2004, *ApJS*, 154, 396

Table 1. SMA Observations of CB 17

Object Name	R.A. & Dec. (J2000) ^a [h : m : s, ° : ' : '']	Distance [pc]	Array configuration	HPBW ^b [arcsec]	rms ^c [mJy beam ⁻¹]
CB 17	04:04:35.85, 56:56:03.09	250	compact	3.1×2.8	0.55, 55 (0.5 km s ⁻¹)

^aPhase center in the SMA observations.

^bRobust (+1.0) weighted synthesized FWHM beam size of the SMA 1.3 mm dust continuum map (combining the 2008 and 2009 LSB data).

^c1 σ theoretical noises of 1.3 mm dust continuum and the ¹²CO (2–1) line (per channel width).

Table 2. *Spitzer* Imaging Sensitivities of CB 17 & L1448^a

Source	IRAC1 (3.6 μ m) [mJy/sr]	IRAC2 (4.5 μ m) [mJy/sr]	IRAC3 (5.8 μ m) [mJy/sr]	IRAC4 (8.0 μ m) [mJy/sr]	MIPS1 (24 μ m) [mJy/sr]	MIPS2 (70 μ m) [mJy/sr]	MIPS3 (160 μ m) [mJy/sr]
CB 17	0.10±0.03	0.17±0.04	0.8±0.1	3.0±0.2	22±0.2	14±2	100±10
L1448	0.20±0.05	0.25±0.05	1.5±0.2	6.5±0.5	36±1.0	20±5	150±20
	[μ Jy/pixel]	[μ Jy/pixel]	[μ Jy/pixel]	[μ Jy/pixel]	[mJy/pixel]	[mJy/pixel]	[mJy/pixel]
CB 17	3.6±1.0	6.1±1.4	29±3	110±7	3.6±0.03	7±1	600±60
L1448	7.2±2.0	9.0±1.8	54±6	240±20	5.9±0.15	10±3	900±90

^a1 σ rms of images near the positions of the two sources.

Table 3. SMA 1.3 mm dust continuum results of CB 17

Source Name	R.A. & Dec. (J2000) [h : m : s, ° : ' : '']	Gaussian Fitting		3 σ Level ^b	
		Flux (mJy)	$M_{\text{gas}}^a (M_{\odot})$	Flux (mJy)	$M_{\text{gas}}^a (M_{\odot})$
CB 17 IRS	04:04:33.76, 56:56:16.5	6.3±1.3	0.023±0.005	5.8±1.2	0.021±0.004
CB 17 MMS	04:04:35.78, 56:56:03.4	3.8±0.7	0.035±0.007	3.5±0.7	0.032±0.006

^aTotal gas mass; See text for dust temperature and opacity used.

^bFlux integrated above the 3 σ level, and corresponding gas mass.

Table 4. Photometry of CB 17 IRS and MMS

λ (μm)	CB 17 IRS		CB 17 MMS	
	S_ν (mJy)	Aperture (arcsec)	S_ν (mJy)	Aperture (arcsec)
2.2	1.1 \pm 0.5	5.0
3.6	1.71 \pm 0.3	2.4	< 0.011 ^a	1.2
4.5	1.78 \pm 0.3	2.4	< 0.018 ^a	1.2
5.8	1.22 \pm 0.3	2.4	< 0.084 ^a	1.2
8.0	0.6 \pm 0.2	2.4	< 0.3 ^a	1.2
24	92 \pm 20	5	< 11 ^a	2.5
60	910 \pm 450	75
70	1130 \pm 220	20	< 90 ^a	20
100	5780 \pm 2000	125	36 \pm 2 ^b	7
160	4300 \pm 1500	40	800 \pm 200	20
450	< 1000 ^c	10	< 800 ^c	10
850	< 120 ^c	14	180 \pm 40 ^c	14
1300	30 \pm 6 ^c	12	50 \pm 10 ^c	12

^aDetection upper limits (3σ per aperture) at the position of CB 17 MMS in the *Spitzer* images.

^bFlux derived from the *Herschel* PACS 100 μm observations (M. Schmalzl et al. in preparation).

^cFlux estimated using dust continuum emission within one beam of CB 17 IRS and MMS in the JCMT/SCUBA and IRAM-30m images.

Table 5. Outflow parameters of CB 17 IRS and MMS^a

Component	Mass [$10^{-3} M_\odot$]	Momentum [$10^{-3} M_\odot \text{ km s}^{-1}$]	Energy [10^{40} ergs]	\dot{M}_{out} [$10^{-8} M_\odot \text{ yr}^{-1}$]	Force [$10^{-8} M_\odot \text{ km s}^{-1} \text{ yr}^{-1}$]	Luminosity [$10^{-5} L_\odot$]
CB 17 IRS blue	0.30	0.75	1.9	2.7	6.8	1.4
CB 17 IRS red	0.22	0.49	1.1	2.0	4.5	0.8
CB 17 MMS blue	0.33	0.84	2.1	2.4	6.0	1.2
CB 17 MMS red	0.46	1.02	2.2	3.3	7.3	1.3

^a Lower limits derived from the SMA CO (2–1) observations.

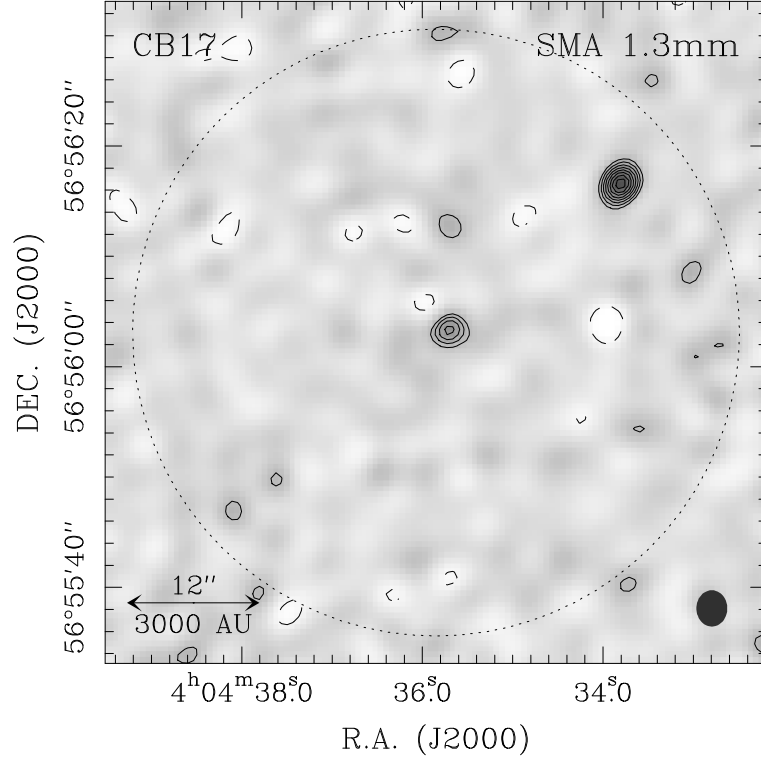


Fig. 1.— The SMA 1.3 mm dust continuum image of CB17, using the data combining the 2008 and 2009 LSB observations. The contours start at $\pm 3\sigma$, and then increase from $+3\sigma$ in steps of 1σ ($\sim 0.55 \text{ mJy beam}^{-1}$). The synthesized SMA beam is shown as a grey oval in the bottom right corner. The dotted circle shows the SMA primary beam size ($\sim 55''$).

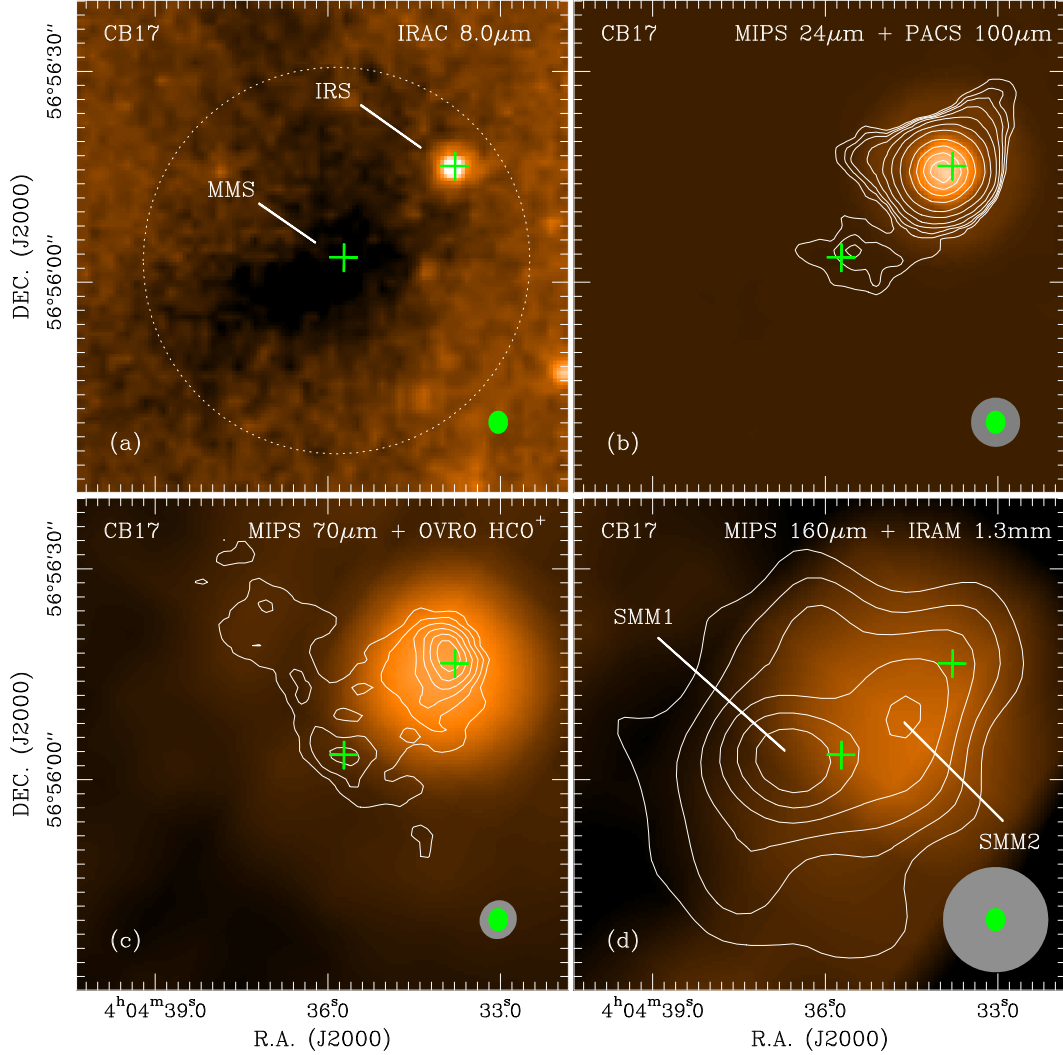


Fig. 2.— *Spitzer* IRAC and MIPS images of CB17. The two green crosses show the positions of the two SMA dust continuum sources (IRS and MMS), and the synthesized SMA beam is shown as a green oval in the bottom right corner. (a) IRAC $8.0\,\mu\text{m}$ image. (b) MIPS $24\,\mu\text{m}$ image, with the *Herschel* PACS $100\,\mu\text{m}$ continuum contours (white) overlapped (data from M. Schmalzl et al., in preparation). The PACS contours correspond to 100, 105, 110, 120, 140, 180, 250 mJy beam^{-1} , and then increase in steps of 150 mJy beam^{-1} . The grey oval in the bottom right corner shows the angular resolution in the PACS $100\,\mu\text{m}$ observations ($\sim 7''$). (c) MIPS $70\,\mu\text{m}$ image, with the OVRO HCO^+ (1–0) emission contours (white) overlapped (data from M. Schmalzl et al., in preparation). The HCO^+ contours (integrated over the velocity from -5.3 to $-4.1\,\text{km s}^{-1}$) start at $\sim 3\sigma$ and then increase in steps of 1σ ($\sim 50\,\text{mJy beam}^{-1}\,\text{km s}^{-1}$). The grey oval in the bottom right corner shows the synthesized OVRO beam size ($\sim 5''$). (d) MIPS $160\,\mu\text{m}$ image, with the IRAM-30m $1.3\,\text{mm}$ dust continuum contours (white) overlapped (data from Launhardt et al. 2010; smoothed to $15''$); the IRAM $1.3\,\text{mm}$ contour values are 20, 26, 32, 38, 44, and 50 mJy beam^{-1} . The grey oval in the bottom right corner shows the smoothed IRAM-30m beam size.

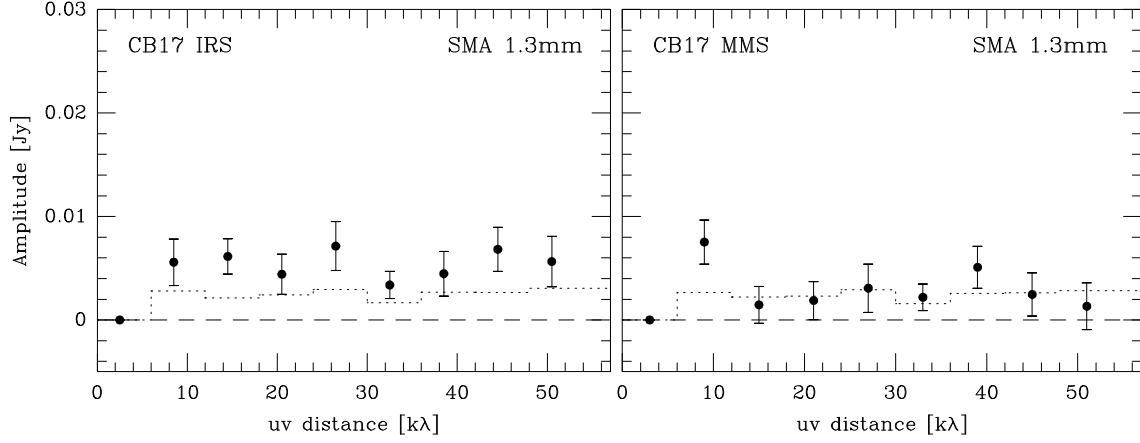


Fig. 3.— Visibility amplitude vs. uv distance plots for the continuum sources CB17 IRS (*Left*) and MMS (*Right*) with 1σ error bars. The dotted histograms are the zero expectation level.

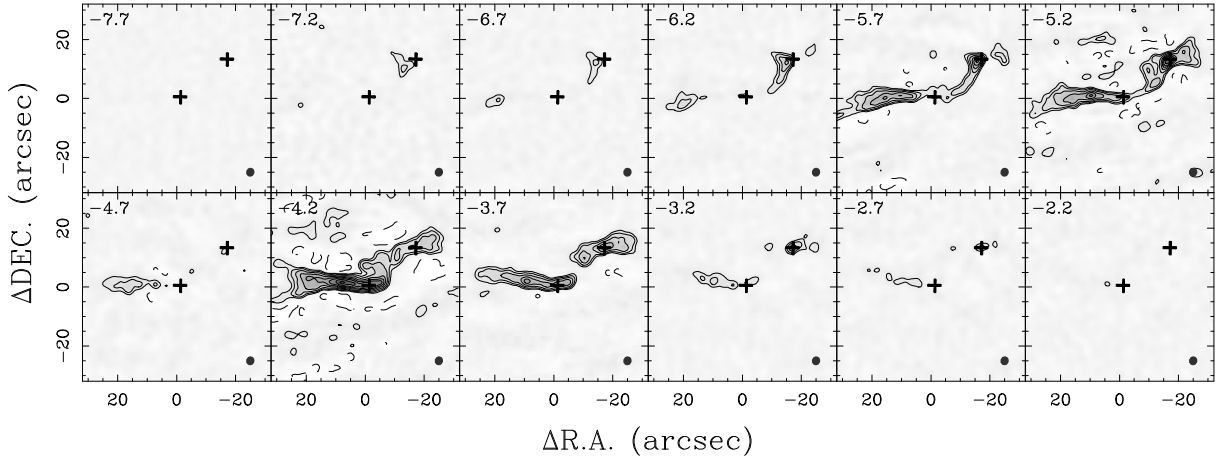


Fig. 4.— Velocity channel maps of the SMA ^{12}CO (2–1) emission of CB17 (phase center R.A. = 04:04:35.85, DEC = 56:56:03.09, J2000). The center velocity of the channel is written in top left corner of each panel (in km s^{-1}). The systemic velocity of the molecular cloud is $\sim -4.7 \text{ km s}^{-1}$. Contours levels correspond to $-3, 3, 5, 8, 12, 16$, and 20σ , then increase in steps of 10σ , where the 1σ level is $\sim 0.1 \text{ Jy beam}^{-1}$. In each panel, the two crosses mark the positions of the two SMA dust continuum sources (CB17 IRS and MMS), while the filled ellipse (lower right corner) indicates the synthesized beam.

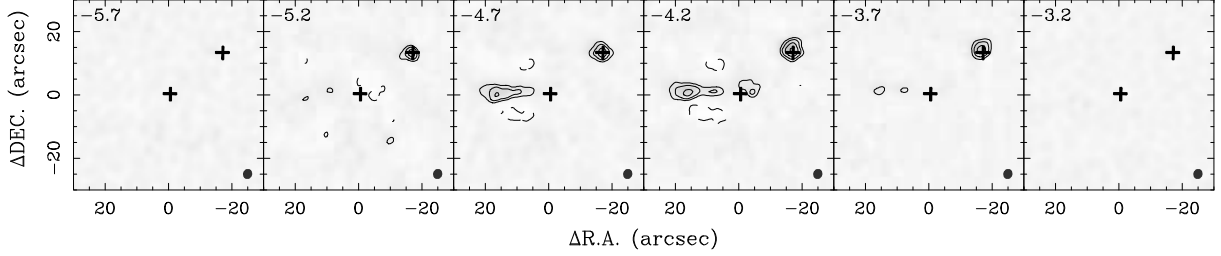


Fig. 5.— Velocity channel maps of the SMA ^{13}CO (2–1) emission of CB 17. Contours levels correspond to $-3, 3, 5, 8, 12, 16$, and 20σ , where the 1σ level is $\sim 0.07 \text{ Jy beam}^{-1}$. In each panel, the crosses mark the positions of the two sources (CB 17 IRS and MMS), while the filled ellipse (lower right corner) indicates the synthesized beam.

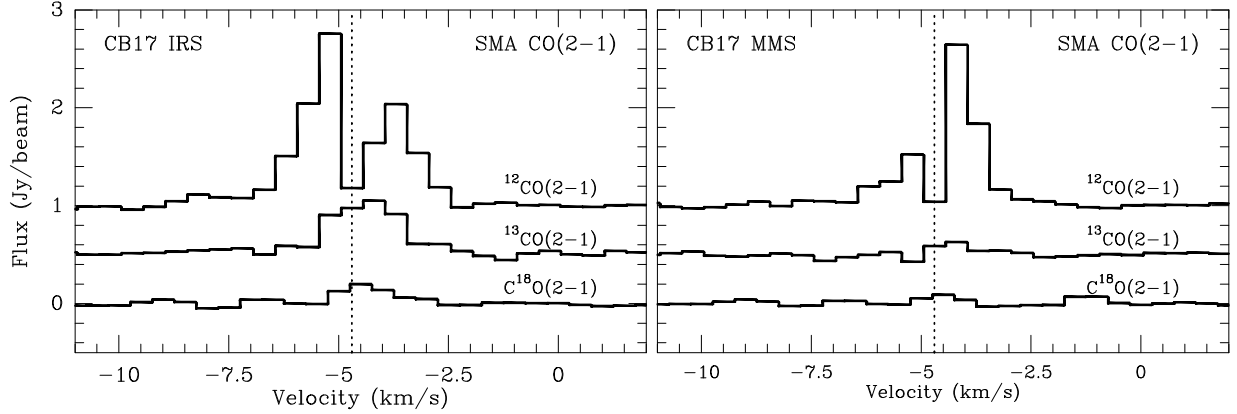


Fig. 6.— SMA CO (2–1) spectra at the peak positions of the continuum sources CB 17 IRS (*left*) and CB 17 MMS (*right*). The SMA spectra shown are obtained by averaging the emission within $3''$ of the peak position (roughly the beam size). The dotted line indicates the cloud systematic velocity derived from the IRAM-30m N_2H^+ (1–0) observations ($\sim 4.7 \text{ km s}^{-1}$).

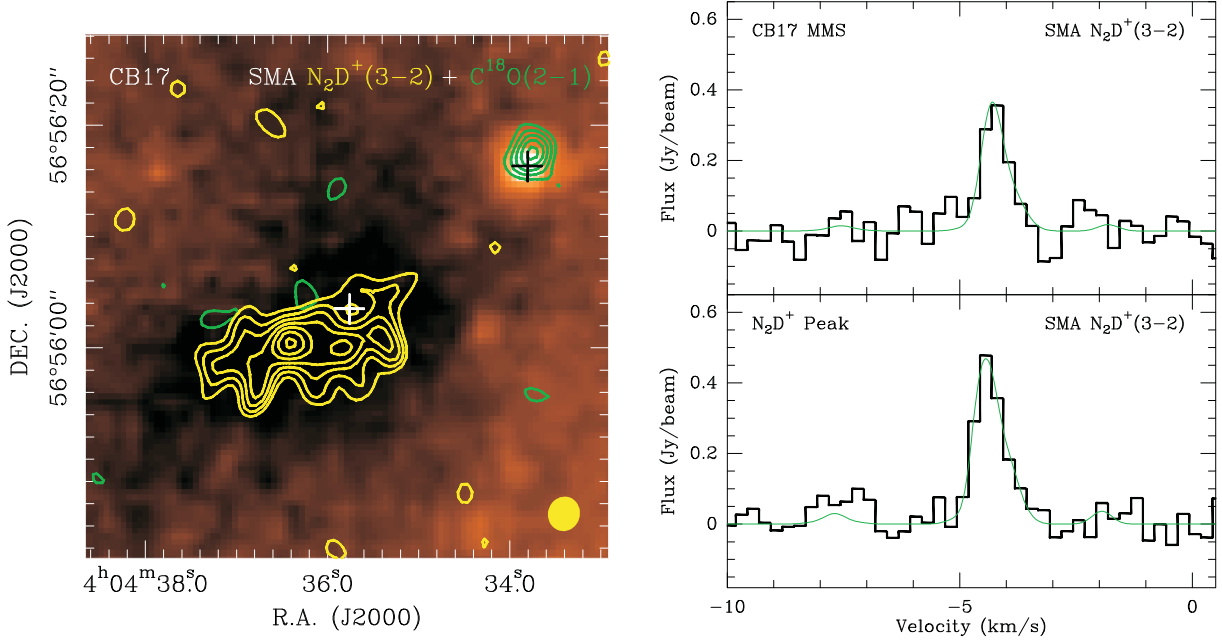


Fig. 7.— *Left*: Velocity-integrated intensity maps of the SMA $\text{N}_2\text{D}^+(3-2)$ emission (yellow contours) and $\text{C}^{18}\text{O}(2-1)$ emission (green contours), plotted on the IRAC $8.0\,\mu\text{m}$ image of CB17. The N_2D^+ and C^{18}O emission is integrated over the velocity from -4.9 to $-3.7\,\text{km s}^{-1}$, and contours start at 3σ and increase in steps of 1σ (~ 0.055 and $\sim 0.070\,\text{Jy beam}^{-1}\,\text{km s}^{-1}$, respectively). The crosses mark the positions of the two continuum sources (CB17 IRS and MMS), while the yellow ellipse indicates the synthesized beam in the $\text{N}_2\text{D}^+(3-2)$ line ($3.1'' \times 2.8''$). *Right*: The $\text{N}_2\text{D}^+(3-2)$ spectrum (histogram) at the position of source CB17 MMS (top) and at the position of the peak integrated intensity (bottom), with a model fit of the $\text{N}_2\text{D}^+(3-2)$ hyperfine structure (continuous line).

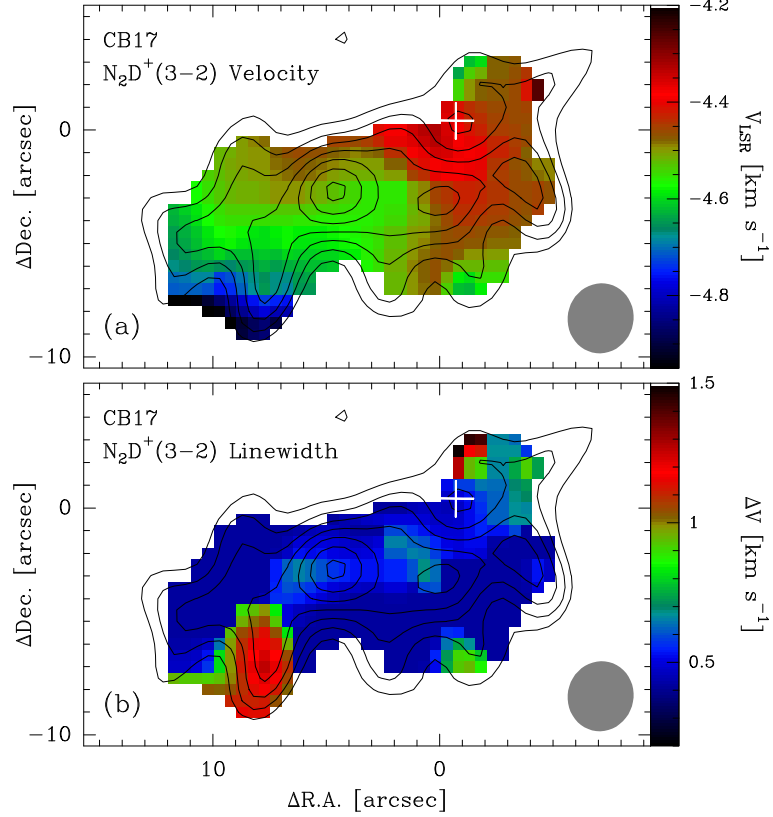


Fig. 8.— $\text{N}_2\text{D}^+(3-2)$ velocity fields of CB17. The top map shows the mean velocity field (color shades), while the bottom map shows the spatial distribution of the $\text{N}_2\text{D}^+(3-2)$ line width (color shades). In both maps, black contours show the integrated intensity (from Figure 7), and the cross shows the position of source CB17 MMS. The SMA synthesized beam in the N_2D^+ observations is shown in the bottom right corner.

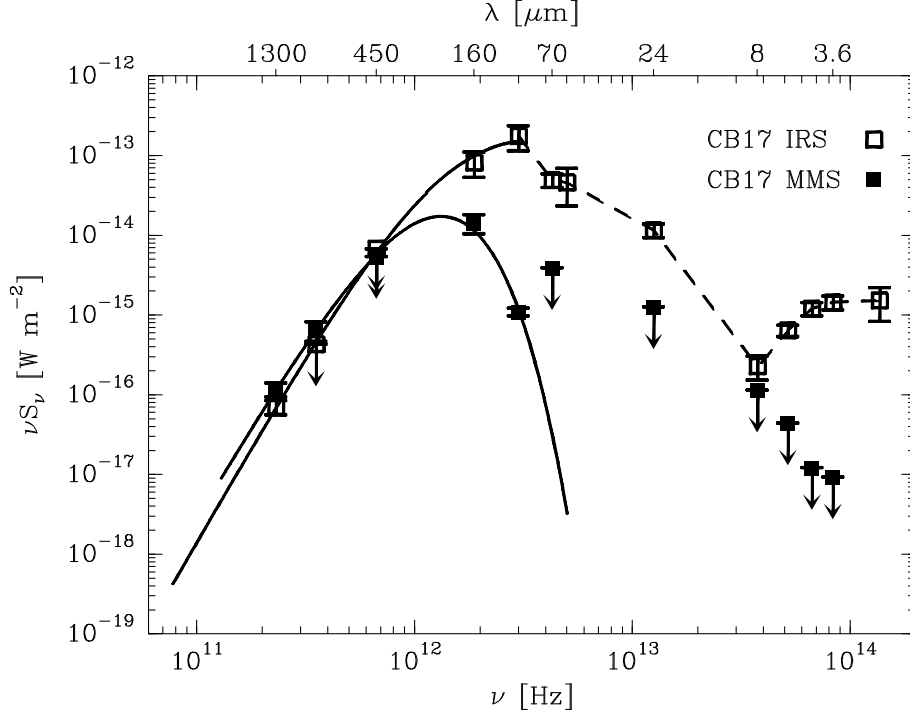


Fig. 9.— Spectral energy distributions of CB 17 IRS and MMS (see Table 4 for the values of individual data points). Solid lines show the best-fit for all points (including upper limits) at $\lambda \geq 100 \mu\text{m}$ using a grey-body model $S_\nu = B_\nu(T_d)(1 - e^{-\tau_\nu})\Omega$, where $B_\nu(T_d)$ is the Planck function at frequency ν and dust temperature T_d , τ_ν is the dust optical depth as a function of frequency $\tau \propto \nu^{1.8}$, and Ω is the solid angle of the source. Dashed line shows a simple logarithmic interpolation performed between all points at $\lambda < 100 \mu\text{m}$ for source CB 17 IRS (not performed for CB 17 MMS).

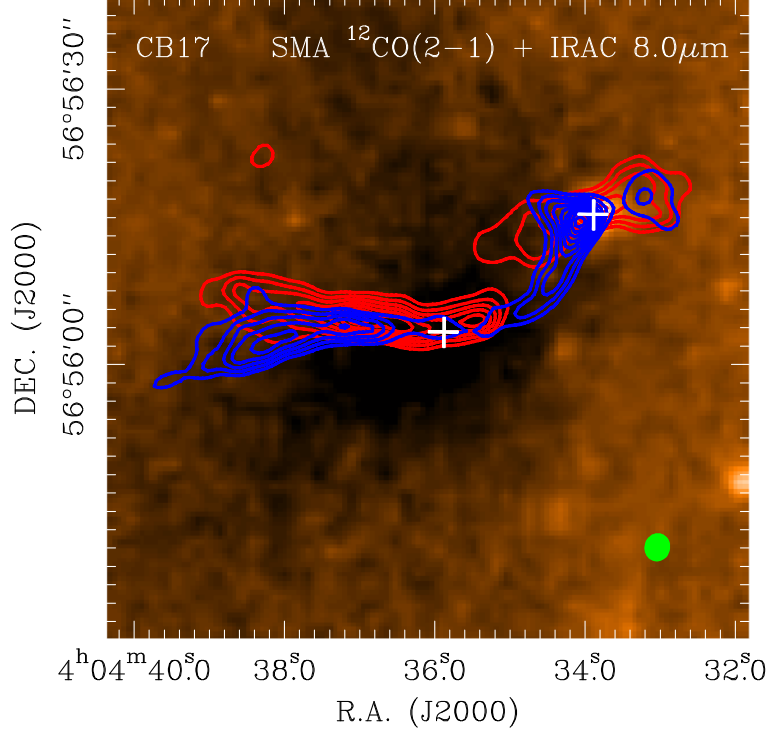


Fig. 10.— The integrated intensity maps of the SMA $^{12}\text{CO}(2-1)$ emission from CB17, plotted on the *Spitzer* IRAC $8.0\,\mu\text{m}$ image. The blue (red) CO contours represent emission integrated over the velocity range $-7.2\,\text{km s}^{-1} < V_{\text{LSR}} < -5.7\,\text{km s}^{-1}$ ($-3.7\,\text{km s}^{-1} < V_{\text{LSR}} < -2.2\,\text{km s}^{-1}$), which is blueshifted (redshifted) with respect to the cloud systemic velocity ($-4.7\,\text{km s}^{-1}$). The CO contours start at $\sim 0.45\,\text{Jy beam}^{-1}\,\text{km s}^{-1}$ ($\sim 3\sigma$), and increase in steps of $0.3\,\text{Jy beam}^{-1}\,\text{km s}^{-1}$ ($\sim 2\sigma$). The two white crosses mark the positions of the two continuum sources (CB17 MMS and IRS), while the green oval in the bottom right corner indicates the SMA synthesized beam (^{12}CO line).

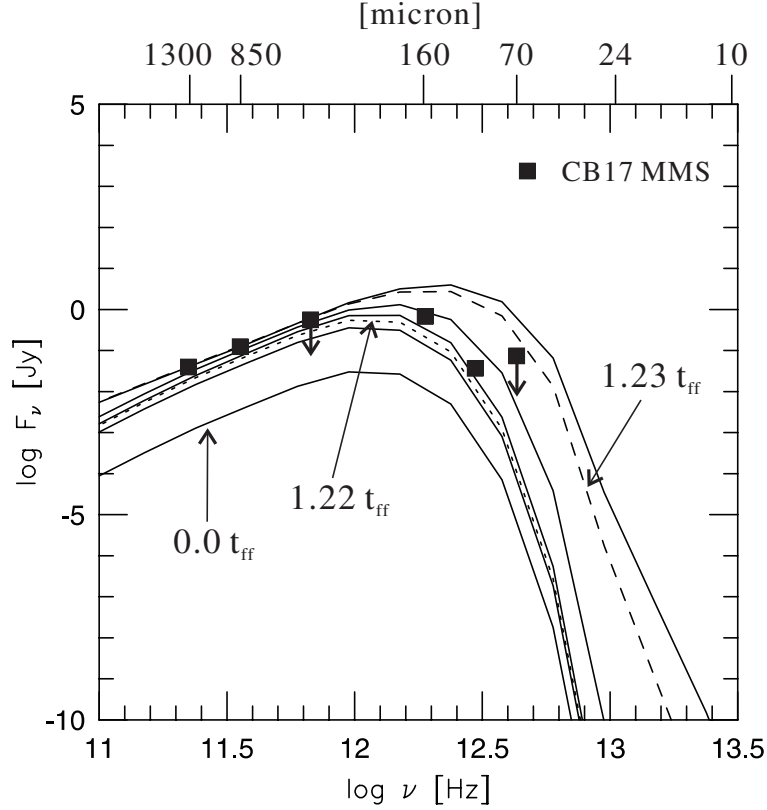


Fig. 11.— Comparison between the fluxes of CB17MMS (see Table 4) and the fluxes expected for a first core at different evolutionary stages (fluxes that would be observed with the beam size of 10^3 AU or $4''$ at the distance of CB17; from the model M1a in Masunaga et al. 1998). The solid, dashed, and dotted lines show the evolution of the SED of a first hydrostatic core with a luminosity of $0.06 L_\odot$ (evolved at $\rho_{\text{center}} \sim 10^{-9} \text{ g cm}^{-3}$ or *time* approximately $1.23 t_{\text{ff}}$), where the t_{ff} is the free-fall time. Note that the beam sizes of SCUBA and IRAM-30m (see Table 4) are larger than the beam size used to derive fluxes in the model.